AIAA 2008-2848

Numerical study of aeroacoustic coupling in a subsonic confined cavity

Thomas Emmert and Philippe Lafon*†

Laboratoire de Mécanique des Structures Industrielles Durables,
UMR CNRS EDF 2832, Clamart, France

Christophe Bailly‡

Laboratoire de Mécanique des Fluides et d'Acoustique,
École Centrale de Lyon & UMR CNRS 5509, Ecully, France

A ducted cavity flow at moderate Mach number is investigated numerically by compressible large-eddy simulation based on explicit filtering of the Navier-Stokes equations and a high-order finite-difference algorithm. Experimental observations reveal that for some particular Mach number values of the free stream, a coupling occurs between the cavity flow and the pressure oscillations in the duct. The present computations retrieve most of the physical phenomena. The lock-in frequencies are well predicted but the amplitude of the oscillations exhibits some discrepancies. Computations on coarse and fine grids show that the hierarchy of the cavity modes is better captured on a finer grid.

I. Introduction

Ducted cavities are well-known configurations of pipe systems with flow control devices or valves, and also in organ pipes or flutes for instance. They generate discrete tones which can be amplified by the natural modes of the pipe structure. Like classical open cavities, ducted cavities underly a feedback mechanism that can be described as follows: Vortical structures develop in the shear layer above the cavity and are convected downstream. The impact of the eddies on the downstream corner lead to pressure perturbations that trigger further instabilities at the upstream cavity corner giving a phase locking of the whole system, known as the Rossiter modes.[1] Additionally in the ducted case, acoustic modes of the duct can also be excited. In the past many experimental and numerical investigations about open cavities were done, especially for predicting resonance frequencies and pressure levels.[2,3]

The configuration considered here has been studied in the context of an industrial application. It has been already studied in 2-D by using a second-order TVD-Euler code.[4,5] Rossiter frequencies were recovered, but turbulent aspects could not be considered due to the inviscid 2-D feature of the simulations. As in the present work computations are fully 3-D and are performed using high order methods for solving Navier-Stokes equations, it is expected that more flow details will be retrieved.

The computational algorithm involving low-dissipative and low-dispersive numerical methods is presented in the first section. In the second section, the studied configuration is presented with emphasis on experimental results and physical mechanisms. In the third section, the simulation parameters are detailed for a coarse grid and for a fine grid. Then in the last section, the results are analysed.

II. Numerical algorithm

The set of equations are the compressible 3-D Navier-Stokes equations, written in conservative form after application of a general time-invariant curvilinear coordinate transformation from physical space to

*Research engineer, AIAA Senior Member
†Professor at Ecole Centrale Lyon and Institut Universitaire de France, AIAA Senior Member

Copyright © 2008 by the authors. Published by the American Institute of Aeronautics and Astronautics, Inc., with permission.

computational space $(x, y, z) \rightarrow (\xi, \eta, \zeta)$. This yields

$$\frac{\partial}{\partial t}\left(\frac{\mathbf{Q}}{J}\right) + \frac{\partial \mathbf{E}}{\partial \xi} + \frac{\partial \mathbf{F}}{\partial \eta} + \frac{\partial \mathbf{G}}{\partial \zeta} = 0,$$

where J is the Jacobian of the geometric transformation. The unknown vector in the above equation writes $\mathbf{Q} = (\rho, \rho u, \rho v, \rho w, \rho e_t)^T$, where ρ designates the density, u, v, w the Cartesian velocity components and ρe_t the total energy. The latter is calculated for a perfect gas such as $\rho e_t = p/(\gamma - 1) + \rho(u^2 + v^2 + w^2)$ with the pressure p. The flux vectors $\mathbf{E}$, $\mathbf{F}$, $\mathbf{G}$ contain the inviscid and the viscous terms. Their expressions as well as the metric identities for the grid transformation can be found in the literature.[6,7]

For interior points of the computational domain, the fluxes and the velocity derivatives for the viscous terms are discretized by the centered 11-point finite difference scheme developed by Bogey & Bailly.[8] This scheme has been optimized in wave number space and is able to resolve accurately perturbations with only four points per wavelength. An explicit fourth-order low-storage Runge-Kutta scheme advances the solution in time. The CFL number is 0.9 and the time step Δt is updated every iteration during the transient phase. An appropriate optimized explicit 11-point low pass filter remove grid-to-grid oscillations, not resolved by centered finite difference schemes.[8] At the same time the filter removes properly the non-resolved turbulent structures and acts like a subgrid scale model. This method has been successfully applied in the literature.[9,10] The filtering coefficient is chosen to be 0.2 inside the computational domain.

The implemented finite difference schemes are limited to structured grids. In order to treat more complex geometries, a high-order overset ability has been adapted and implemented in the code. In this approach the computational domain is subdivided into overlapping structured grid components. The governing equations are solved on each component grid separately and domain connectivity is obtained through the use of interpolation. Also known as the Chimera grid method, this approach has been proposed first for aerodynamics[11] and extended later for aeroacoustic simulations.[12] For grid generation *ogen*, the grid assembler module of the freely available library *Overture*[13] developed at the Lawrence Livermore National Laboratory, has been interfaced with the code. For communication between grid boundaries that do not coincide, high-order interpolation is used. Lagrangian polynomials has been found to be best suited in terms of precision, execution time and implementation aspects for the high-order overset grid approach.[14] Various tests have shown that at least eight-order polynomials have to be used in order to make the error of the interpolation negligible when using the 11-points difference scheme. For load balancing purpose, each component grid can be subdivided evenly N times in each direction and can be computed by $N_{\text{procs}} = N_{\xi,\text{procs}} \times N_{\eta,\text{procs}} \times N_{\zeta,\text{procs}}$. The standard Message Passing Interface (MPI) library routines have been used for code parallelization.

All the aforementioned characteristics have been implemented in a numerical solver of the Navier-Stokes equations, called SAFARI (Simulation of Aeroacoustic Flows And Resonance and Interaction). Details can be found in a companion paper.[15]

III. Experimental observations

Ducted cavities have first been studied for an industrial application: a pure tone phenomenon was observed on the power steam line of a nuclear power station.[4] A cavity located in a gate valve was identified as the source. This cavity has two characteristics that are different from the classical cavities often considered in the literature: it is placed in a duct and it is partially covered.

It is well known that a flow past a cavity gives rise to noise radiation. A complex feed back process between the upstream and downstream corners produces coherent oscillations in the shear layer developing above the cavity.[16–18] For cavities in open space, the oscillations remain weak at low Mach numbers. Therefore most published papers are concerned by Mach number range in the high subsonic domain. For ducted cavities, the possible coupling between cavity oscillations modes and duct acoustic modes can lead to high amplitude oscillations at even low speeds.

The real geometry of the valve is quite complex and a simplified plane geometry was retained in order to study the complex physical phenomena. This geometry is displayed in Figure 1. The experimental results obtained in the previous studies[4,19] are now used as validation data for the capability of numerical tools to capture the flow acoustic phenomenon in such configuration.

Details about the experiments are given in previous papers.[4,19] The main outlines are recalled here. The characteristic dimensions of the experimental model are : $d = 0.05$ m, $h = 0.02$ m, $H = 0.137$ m,

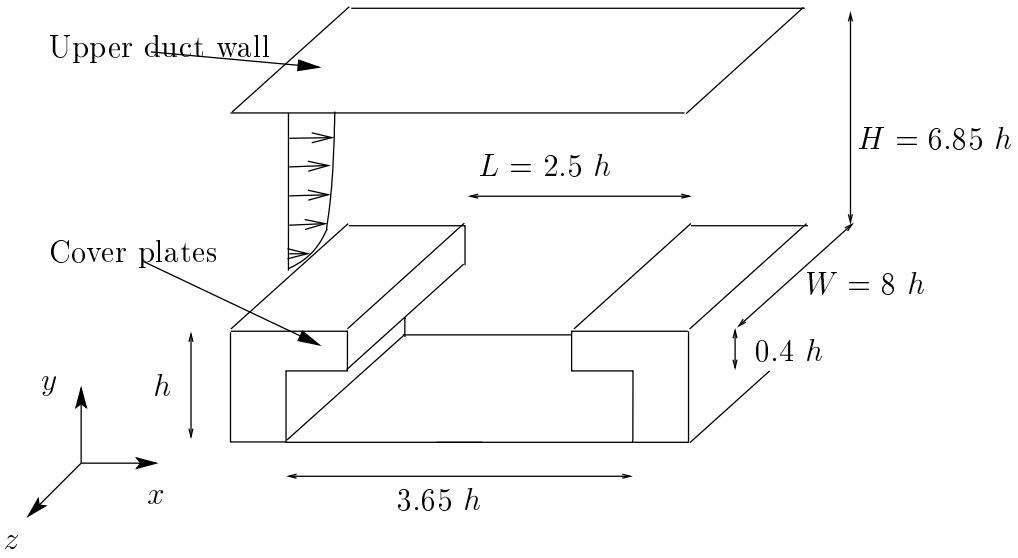

Figure 1. Ducted cavity: sketch of the geometry and notations $h = 0.02$ m, $d = 0.05$ m, $H = 0.137$ m, $L = 0.073$ m and $W = 0.16$ m. The aspect ratio of the cavity is $L/D = 2.5$. U_0 is the free stream velocity.

$L = 0.073$ m. The span of the test section has a value of 0.16 m. The measurements were made using a microphone located at the bottom center of the cavity. The measured spectra exhibit peaks that can be associated to cavity modes. Plots of frequency and pressure level of these peaks as functions of the nominal Mach number $M_0 = U_0/c_0$ are shown in Figure 2 and Figure 3. The modes 2 and 3 of cavity are given by Rossiter's formula:[1]

$$St_R = \frac{fd}{U_0} = \frac{n_R - \xi}{M_0 + U_0/U_c},$$

where $\xi = 0.25$, $U_0/U_c = 0.57$, and n_R is the mode number. The transverse mode of the duct are given by

$$St_d = f_d \frac{d}{U_0} = \frac{c}{2n_d H} \frac{d}{U_0},$$

where n_d is the duct mode number. In Figure 2, the frequency of the oscillation lock-in the frequency of the pipe mode when Rossiter's mode approaches the duct mode. When lock-in occurs, the pressure level is maximum. At $M = 0.13$, the cavity mode 3 locks with the first transverse duct mode and at $M = 0.18$, the cavity mode 2 locks with the first transverse duct mode. At $M = 0.23$, the cavity mode 3 locks with the second transverse duct mode.

IV. Simulation parameters

IV.A. Coarse grid

The entire grid generated by *ogen* is displayed in Figure 4. It consists of seven component grids. As the grid points of the communication interfaces coincide, no interpolation has to be used. The grid spacing is kept constant in the cavity ($\Delta x = 4\times10^{-4}$ m and $\Delta y = 2\times10^{-4}$ m) and in the boundary layer ($\Delta y = 2\times10^{-4}$ m). In the duct, the grid is stretched in the y-direction near the upper wall with 3.0%. Upstream and downstream of the cavity the grid is stretched in the x direction with 1.0%.

	N_x	N_y	N_z	N_{procs}
Duct	542	149	31	39
Neck	126	39	31	3
Cavity	180	61	31	5

Table 1. Grid parameters for then coarse grid. The case has been computed by $N_{\text{procs}} = 47$ processors. The total number of grid points is 6×10^6.

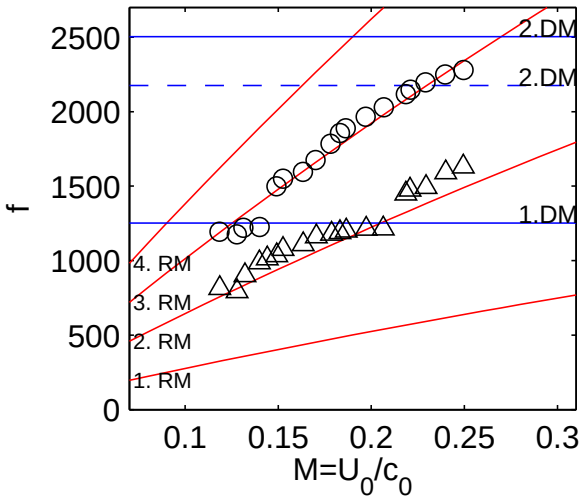

Figure 2. Frequency of dominant pressure spectra peaks (△, ○) measured inside the cavity compared to theoretical ones as a function of the Mach number U_0/c_0: —— theoretical Rossiter mode for $n_R = 1, 2, 3, 4$; —— acoustic transverse duct modes $n_D = 1, 2$ based on duct height H ; - - - - acoustic transverse duct modes $n_D = 2$ based on duct height and cavity height $H + h$.

IV.B. Fine grid

The fine grid generated by *ogen* is displayed in Figure 5. Only the component grids are shown. For the component grids close to the lower boundaries, the points at communication interfaces coincide as for the coarse grid. But the two duct grids (the intermediate one and the main one) are true overlapping grids for which the overset strategy implemented in SAFARI code is required. Figure 6 displays a view of the overlapping zone between the two duct grids. The fine grid consists of eleven component grids. The grid spacing is kept constant in the cavity ($\Delta x = 1.4 \times 10^{-4}$ m and $\Delta y = 1 \times 10^{-4}$ m) and in the boundary layer ($\Delta y = 1 \times 10^{-4}$ m). In the duct, there is no grid stretching in the y-direction. Upstream and downstream of the cavity the grid is stretched in the x direction with 1.0%.

	N_x	N_y	N_z	N_{procs}
Duct	453	94	61	14
Intermediate	1583	86	61	36
Boundary layer	2025	173	61	126
Neck	358	79	61	8
Cavity	521	120	61	22

Table 2. Grid parameters for the fine grid. The case has been computed by $N_{\text{procs}} = 206$ processors. The total number of grid points is 38×10^6.

IV.C. Boundary conditions

One of the crucial points in cavity simulations is the boundary layer upstream the cavity, whose shape controls the vortex shedding and the convection of the eddies in the shear layer. The boundary layer profile that was measured experimentally is fitted in a $1/n$ profile such as:

$$\frac{u_b(y)}{U_0} = \left(\frac{y}{\delta}\right)^{\frac{1}{n}},$$

where $\delta = 8.8$ mm and $n = 8.5$. A friction velocity $u_f = 2.65$ m/s has been estimated yielding a $\Delta y^+ = 23$ for the coarse grid.

This measured profile is imposed as initial condition. During the simulation the profile is recalled along the inlet boundary condition through the weak expression:

$$u^{n+1} = u^{n+1} - \sigma_{rc}(u^{n+1} - u_b(y)),$$

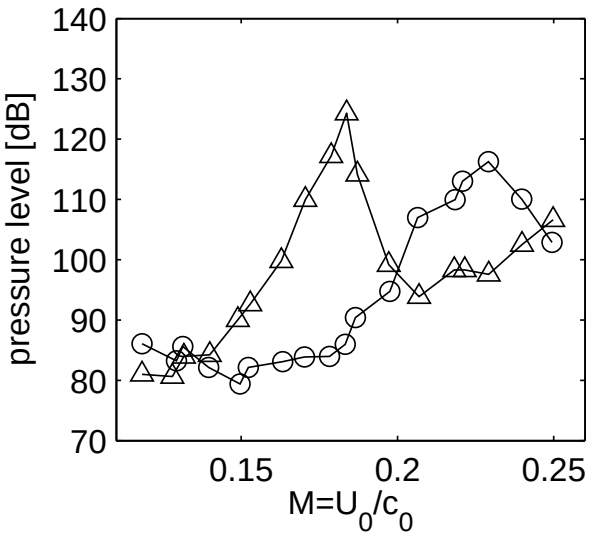

Figure 3. Sound pressure levels of main pressure spectra peaks (△, ○) measured inside the cavity as a function of the Mach number .

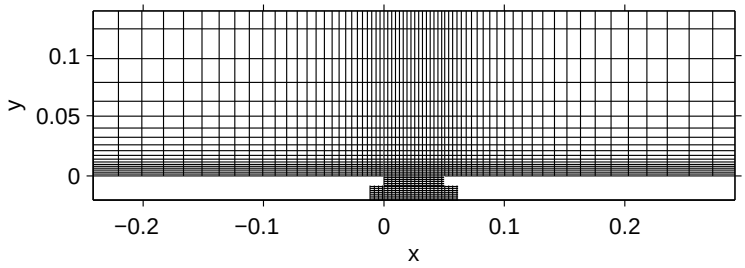

Figure 4. Coarse grid generated by *ogen*. Every tenth line is represented.

where $\sigma_{rc} = 0.005$ has to be kept small in order to avoid numerical reflections.

When the first computations were made, the experimental profile was imposed at the inlet as the boundary condition. It turned out that this profile was not stable and so was rather modified compared to the measured one. The boundary layer is under-resolved and cannot be accurately captured using a coarse grid. Further investigations should be carried out with a finer grid for the upstream boundary layer. But as the main goal of this work is to study the turbulent flow at the cavity and the acoustic coupling with the duct, the experimental profile has been imposed at the inflow boundary. At each time step, this mean flow is substracted from the computed instantaneous flow field in order to obtained the fluctuations. And only these fluctuations are filtered by the numerical algorithm. This technique avoid excessive filtering of the inflow velocity profile and he initial mean flow field is preserved during the simulation run.

As the flow is in the low subsonic domain, the density and the pressure are taken constant over the whole height of the inflow and outflow ($p_{in} = p_{out} = 10^5$ N/m^2, $\rho_{in} = \rho_{out} = 1.2$ kg/m^3). Like for the velocity profile, the density and the pressure are imposed in a weak manner in order to avoid numerical drift. An sponge zone combining grid stretching and a Laplacian filter at the outflow are used to avoid reflections.

V. Results on the coarse grid

Calculations have been carried out on the coarse grid for several nominal Mach numbers : 0.13, 0.16, 0.18, 0.20, 0.21, 0.23, 0.25. The numerical spectra obtained from signals recorded at the bottom center of the cavity, as for the experiments, give the frequency and the amplitude of the peaks associated to the second and third cavity Rossiter's modes.

Figure 7 shows the evolution of the computed and measured frequencies of the two modes. The frequencies are well retrieved. The lock-in phenomenon can be observed when the frequencies of cavity modes stops

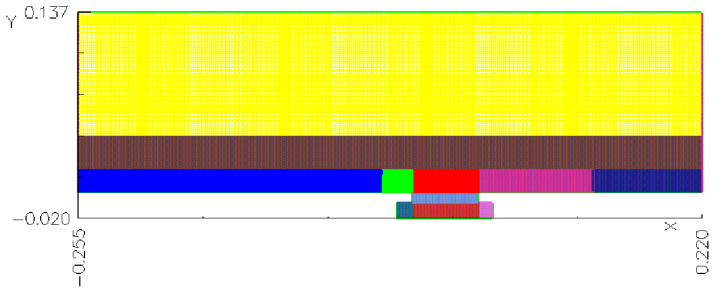

Figure 5. Fine grid generated by *ogen*. Only the component grids are shown.

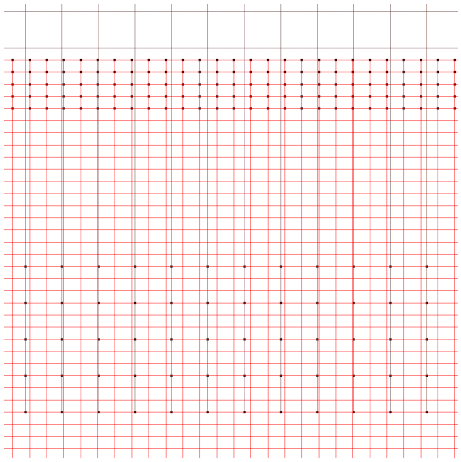

Figure 6. View of an overlapping zone for the fine grid.

their natural evolution and remain locked to the duct mode: at $M = 0.13$, lock-in between modes 3.RM and 1.DM, at $M = 0.18/0.20$, lock-in between modes 2.RM and 1.DM and at $M = 0.23/0.25$, lock-in between modes 3.RM and 2.DM occurs. In the latter case, it is observed that the lock-in phenomenon occurs rather with the 2.DM mode based on the sum of the duct and cavity height. This is consistent with experimental results.

Figure 8 shows the evolution of the computed and measured amplitudes of the cavity modes. The comparison is qualitatively good. But the mode 2.RM remains too high after lock-in having occured at $M = 0.18/0.20$. The amplitude of 3.RM is too high for low Mach numbers and too low for high Mach numbers. As a consequence, the crossing of the amplitude curves of modes 2.RM and 3.RM at $M = 0.2$ is not reproduced.

Figures 9, 10, 11 show snapshots of the instantaneous pressure field in the duct and vorticity field in the cavity. Figure 10 shows that at $M = 0.18$, when the mode 2.RM dominates the spectrum, two eddies appear very distinctly in the shear layer. In Figures 9 and 11, the conclusion is less obvious, because for these two Mach numbers, the 2. and the 3. Rossiter modes are closer. It seems however that the 3.RM appears with three eddies in the shear layer.

These results show that is possible to reproduce the coupling lock-in phenomenon between the cavity modes and the duct modes with the present numerical algorithm. Qualitative discrepancies, in particular the absence of a dominant 3.RM cavity mode for mach numbers higher than 0.2, need to be clarified. That is why computations on a fine grid have been carried out.

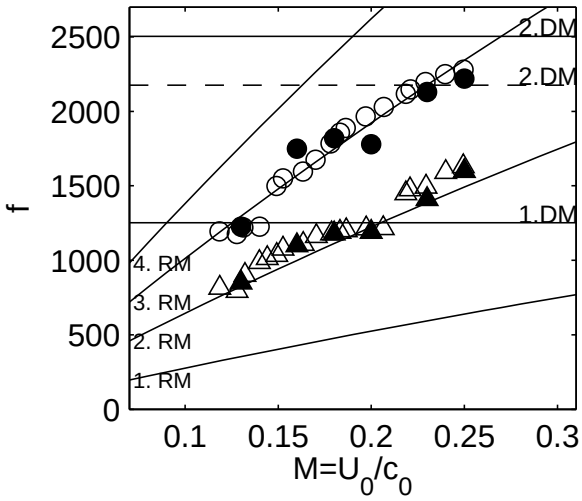

Figure 7. Computed frequencies (mode 2, ▲, mode 3, •) of the cavity modes compared to experimental ones (mode 2, △, mode 3, ○) and to Rossiter's and duct mode frequencies (RM = Rossiter's mode, DM = duct modes). The modified 2.DM mode is calculated with the sum of the duct and the cavity heights .

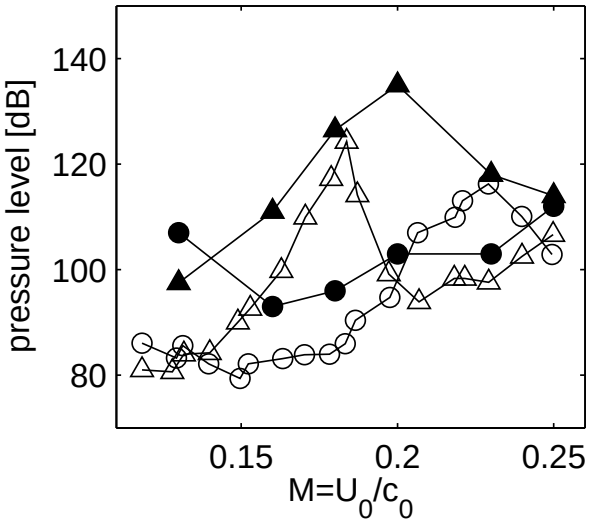

Figure 8. Computed power levels (mode 2, ▲, mode 3, •) of the cavity modes compared to experimental ones (mode 2, △, mode 3, ○).

(a)

(b)

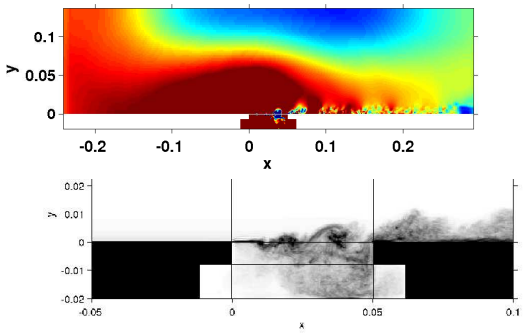

Figure 9. Computed instantaneous results for M=0.13 (a) pressure fluctuations (<100 Pa) in the duct, (b) spanwise averaged vorticity modulus in the cavity

(a)

(b)

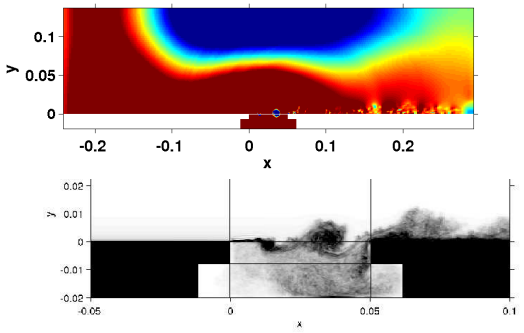

Figure 10. Computed instantaneous results for M=0.18 (a) pressure fluctuations (<100 Pa) in the duct, (b) spanwise averaged vorticity modulus in the cavity

(a)

(b)

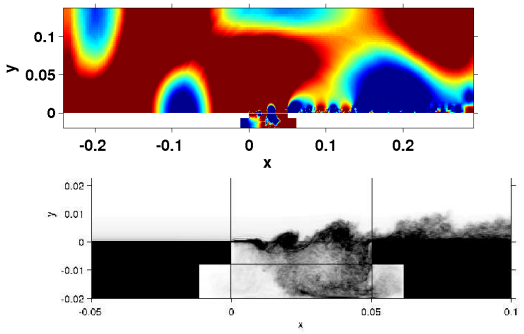

Figure 11. Computed instantaneous results for M=0.23 (a) pressure fluctuations (<100 Pa) in the duct, (b) spanwise averaged vorticity modulus in the cavity

VI. Results on the fine grid

Figures 12 and 13 displays comparison of the spectra obtained on the coarse grid and on the fine grid for the two Mach numbers of 0.18 and 0.23. For $M = 0.18$, Figure 12 shows that computations on the two grids give very close results. The lock-in between the second Rossiter mode and the first transverse duct mode at $f = 1200$ Hz is clearly observed. The third Rossiter ($f = 1800$ Hz) and the second harmonics at ($f = 2400$ Hz) are present but very weak.

For $M = 0.23$, noticeable differences between computations on the two grids are observed in Figure 13. The second Rossiter mode is still higher than the third one but the gap is reduced. It appears also that as the second Rossiter mode decreases ($f = 1400$ Hz), the first tranverse mode ($f = 1200$ Hz) peak increases. It seems that a transfer from a situation where the lock-in between the 2.RM and 1.DM was still dominating to a situation where the lock-in beetween 3.RM and 2.DM is becoming more powerful, is occurring.

But not only the grid has changed. In section IV.C, when presenting the boundary conditions treatment, it is emphasized that the boundary layer upstream the cavity is computed in such a way that the mean experimental profile is used for obtaining the fluctuations. So, the mean experimental profile is imposed upstream the cavity. That is the case for the coarse grid computations. But this approach seemed too crude and could block the evolution of the shear layer and the cavity modes. So, for the fine grid computations, the component grid just upstream the cavity (see Figure 5) is treated without imposing the mean experimental profile. Then, just upstream the cavity, the flow is free to adapt with respect to downstream perturbations.

It appears now that it is difficult to conclude whether it is the finer grid or the boundary layer treatment that explains result improvement.

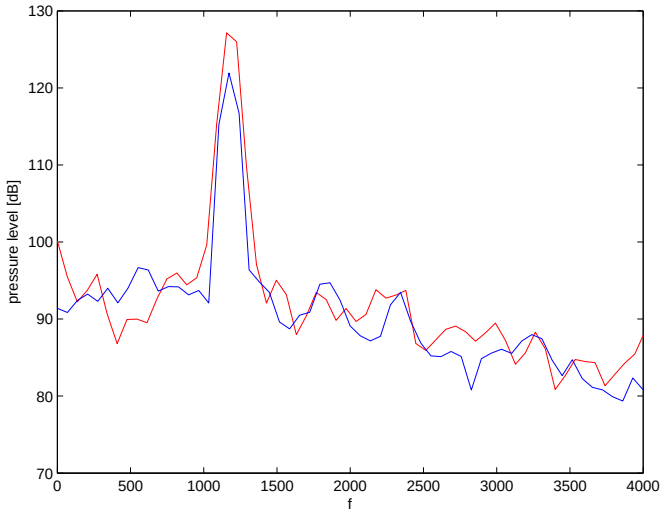

Figure 12. Computed spectra at $M = 0.18$ for the coarse grid (blue curve) and for the fine grid (red curve).

VII. Conclusion

The problem of flow/acoustic coupling in ducted cavity configurations has been studied using high order numerical methods for solving Navier-Stokes equations.

A first set of results have been obtained on a coarse grid. It is shown that lock-in frequencies are well predicted but the amplitude of the oscillation exhibits some discrepancies. In particular, for Mach numbers higher than 0.2, the second cavity mode remains too high and the third cavity mode too low.

A second set of results have been obtained on a finer grid. The hierarchy of modes for Mach numbers higher than 0.2 is improved. New investigations are needed in order to determine if this improvement is due to the finer grid or to the modification of the boundary layer treatment upstream the cavity.

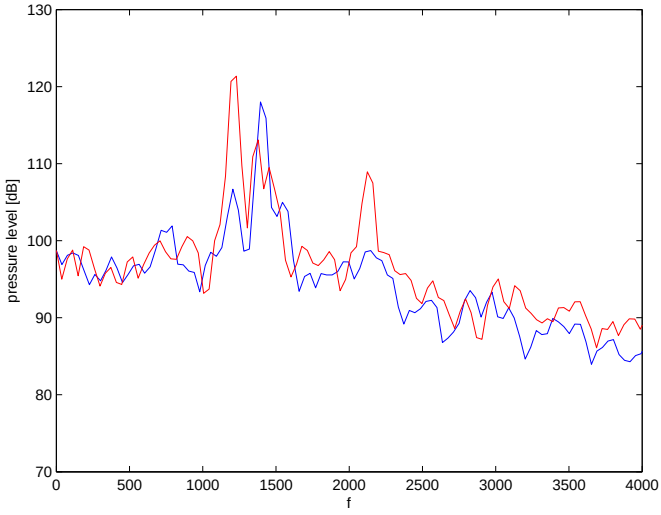

Figure 13. Computed spectra at $M = 0.23$ for the coarse grid (blue curve) and for the fine grid (red curve).

Acknowledgments

Thanks to William Henshaw (Lawrence Livermore National Laboratory) for providing useful advices about the *Overture* library.

References

[1]Rossiter C.W. *Wind-tunnel experiments in the flow over rectangular cavities at subsonic and transsonic speeds.* Aeronautical Research Council Reports and Memoranda, Technical Report 3438.

[2]Rockwell D., Naudascher E. *Self-sustained oscillations of impinging free shear layer.* Annual Review of Fluid Mechanics, **11** (1997) 67-94.

[3]Gloerfelt X., Bailly C. and Juvé D. *Direct computation of the noise radiated by a subsonic cavity flow and application of integral methods.* Journal of Sound and Vibration, **266**(1) (2003), 119-146.

[4]Lafon P., Caillaud S., Devos J.P. and Lambert C. *Aeroacoustical coupling in a ducted shallow cavity and fluid-structure effects on a steam line.* Journal of Fluids and Structures, **18** (2003) 695-713.

[5]Lafon P., Devos J. P. *Computation of the noise generated by a shallow cavity and test of a solution for lowering the noise.* AAIA Paper, (2003) 2003-3105.

[6]Visbal M.R., Gaitonde D.V. *On the use of higher-order finite-difference schemes on curvilinear and deforming meshes.* Journal of Computational Physics, **181** (2002), 155-185.

[7]Marsden O., Bogey C. and Bailly C. *High-order curvilinear simulations of flows around non-cartesian bodies.* Journal of Computational Acoustics, **13**(4) (2005), 732-748.

[8]Bogey C., Bailly C. and Juvé D. *A family of low dispersive and low dissipative schemes for Large Eddy simulations and for sound propagation.* Journal of Computational Physics, **194** (2004), 194-214.

[9]Bogey C., Bailly C. *Large Eddy Simulations of transitional round jets : influence of the Reynolds number on flow development and energy dissipation.* Physics of Fluids, **18** (2006), 1-14.

[10]Gaitonde D.V., Visbal M.R. *Advances in the application of high-order techniques in simulation of multi-disciplinary phenomena.* International Journal of Computational Fluid Dynamics, **17** (2003), 95-106.

[11]Benek J.A., Steger J.L. and Dougherty F.C. *A flexible grid embedding technique with applications to the Euler equations.* AIAA Paper, 83-1944 (1983).

[12]Delfs J.W. *An overlapped grid technique for high resolution CAA schemes for complex geometries.* AIAA Paper, 2001-2199.

[13]Henshaw W. D. *Ogen: an overlapping grid generator for Overture.* http://www.llnl.gov/casc/Overture.

[14]Sherer S.E., Scott J.N. *High-order compact finite-difference methods on general overset grids.* Journal of Computational Physics, **210** (2005), 459 - 496.

[15]Daude F., Emmert T., Lafon P., Crouzet F. and Bailly C. *A high-order algorithm for compressible LES in CAA applications.* AIAA Paper, 2008-3049.

[16]Rockwell D. *Oscillations of impinging shear layers.* AIAA Journal, **21** (1983) 645-664.

[17]Shieh C. M., Morris P. J. *Parallel computational aeroacoustic simulation of turbulent subsonic cavity flow.* AIAA Paper, (2000) 2000-1914.

[18]Bogey C. Gloerfelt X. and Bailly C. *Numerical evidence of mode switching in the flow-induced oscillations by a cavity.* International Journal of Aeroacoustics, **2**(2) (2003), 99-124.

[19]Amandolese X., Hemon P., and Regardin C. *Study of the acoustic oscillations by flows over cavities. Part1. Internals flows.* Proceedings of the Fifth International Symposium on Fluid-Structure Interactions, IMECE'02, New Orleans, (2002).